Available online at www.sciencedirect.com

SCIENCE DIRECT®

Planetary and Space Science 52 (2004) 385–395

Planetary and Space Science

www.elsevier.com/locate/pss

# Identification of the 10-μm ammonia ice feature on Jupiter

Michael H. Wong*,[1], Gordon L. Bjoraker, Michael D. Smith, F. Michael Flasar, Conor A. Nixon

*Laboratory for Extraterrestrial Physics, NASA Goddard Space Flight Center Code 690, Greenbelt, MD 20771, USA*

Received 8 January 2003; accepted 3 June 2003

**Abstract**

We present the first detection of $NH_3$ ice in the thermal infrared in Jupiter's atmosphere using Cassini CIRS observations in the 10-μm region obtained on 31 December 2000 and 1 January 2001.

We identify a brightness temperature difference $\alpha \equiv T_B(1040\ \mathrm{cm}^{-1}) - T_B(1060\ \mathrm{cm}^{-1})$ as an indicator of spectrally identifiable $NH_3$ ice, where 1040 $\mathrm{cm}^{-1}$ is an adjacent continuum region and 1060 $\mathrm{cm}^{-1}$ is the $NH_3$ ice feature. Higher values of $\alpha$ imply a stronger $NH_3$ ice signature in the spectrum. Using midlatitude zonally averaged CIRS spectra, we demonstrate systematic spatial variations in $\alpha$, with the highest values at the equator and near 23°N.

In one CIRS spectral average (covering 22–25°N and 140–240°W), our radiative transfer models are consistent with an optical depth of $0.75 \pm 0.25$ for $NH_3$ ice particles modeled as randomly oriented 4:1 prolate spheroids (volume equivalent radius = 0.79 μm). Particles larger or smaller than 1 μm by about a factor of 2 would be unable to duplicate the observed $NH_3$ ice feature at 1060 $\mathrm{cm}^{-1}$: absorption due to larger particles is excessively broadened, and absorption due to smaller particles is hidden by $NH_3$ gas absorption at 1067 $\mathrm{cm}^{-1}$. We also modeled an average spectrum for a second region on Jupiter (14–17°N and 10–70°W), finding an upper limit of $\tau = 0.2$ for the same $NH_3$ ice particle type. The choice of prolate spheroid particles is based on laboratory studies of $NH_3$ ice aerosols, although 1-μm Mie-scattering spheres would also have detectable signatures at 1060 $\mathrm{cm}^{-1}$. We model the 1-μm $NH_3$ ice cloud with a particle-to-gas scale height ratio $H_p/H_g = 1$. For both CIRS spectra analyzed, the spectrum at frequencies greater than 1100 $\mathrm{cm}^{-1}$ also requires a second cloud with essentially grey absorption, which we modeled using 10-μm $NH_3$ ice spheres distributed with $H_p/H_g = 1/8$ and a cloud base at 790 mbar.

*Keywords:* Atmospheres; Cassini; Ices; Infared spectroscopy

## 1. Introduction

Jupiter is wrapped in clouds at the correct pressure and temperature to be ammonia ice, based on thermochemical models such as Weidenschilling and Lewis (1973) and Atreya et al. (1997). However, spectroscopic proof that this nearly ubiquitous cloud deck is composed of ammonia has been difficult to obtain. Ammonia ice can be identified by two infrared absorption features: the $v_3$ absorption band (N–H stretch) at 2.96 μm (3376 $\mathrm{cm}^{-1}$) and the $v_2$ absorption band (N–H bend) at 9.46 μm (1057 $\mathrm{cm}^{-1}$). Neither $NH_3$ ice feature can be detected from the ground, due to terrestrial $CO_2$ and $H_2O$ absorption at 3 μm and terrestrial ozone absorption at 10 μm.

The expression of the $v_2$ and $v_3$ ammonia ice absorption bands in Jupiter's infrared spectrum is strongly dependent on particle size. Small particles ($r < 1$ μm) have sharply peaked absorption features, but as particle size increases, the absorption feature rapidly broadens. A broadened 3-μm feature has been invoked to explain ISO (Brooke et al., 1998) and Galileo NIMS (Baines et al., 2002) observations. Brooke et al. (1998) analyzed an ISO–SWS reflectance spectrum that covered a quarter of the Jovian disk and ranged from 36°S to 33°N, and they found that a cloud containing approximately unit optical depth of 10-μm ammonia ice spheres gave the best fit to the spectrum between 2.85 and 3.15 μm. The high spatial resolution of NIMS allowed Baines et al. (2002) to map an anomalously low reflectance in the 2.74-μm channel, which they use as the indicator of a spectrally identifiable ammonia

---

* Corresponding author. Tel.: +1-510-642-0388; fax: +1-510-642-3411.

*E-mail address:* mikewong@astro.berkeley.edu (M.H. Wong).

[1] Now at: Astronomy Department, University of California, Berkeley, CA 94720-3411, USA

0032-0633/$ - see front matter © 2003 Elsevier Ltd. All rights reserved.
doi:10.1016/j.pss.2003.06.005

ice cloud. They found these clouds to occupy less than 1% of the globe, primarily at 2–7°N and in the wake of the Great Red Spot. The 3-μm detection of $NH_3$ ice in a disk-averaged spectrum by Brooke et al. (1998) and the 1% $NH_3$ ice coverage noted by Baines et al. (2002) are not necessarily contradictions; the two investigations based their $NH_3$ ice detections on different wavelengths and thus may be sensitive to different particle types and vertical distributions.

Shaffer et al. (1985, 1986) searched Voyager IRIS data for the 10-μm $NH_3$ ice feature, but did not detect it in their averaged spectrum of the North Tropical Zone (about 15–23°N during the Voyager 1 encounter, according to Smith et al., 1979). However, Shaffer et al. (1986) achieved a good fit to the spectrum with $NH_3$ ice particles having a mean radius of 3 μm. These particles are too large to show a strong $NH_3$ ice $v_2$ absorption feature. An analysis of Voyager IRIS spectra in the Equatorial Zone (15°S–15°N) by Marten et al. (1981) also did not detect the 10-μm $NH_3$ ice feature.

Our detection of $NH_3$ ice relies on the identification of a feature with a spectral width of only about 10 $\text{cm}^{-1}$ (0.1 μm). This discrete spectral feature allows an unambiguous determination that the aerosol composition is ammonia, thus confirming thermodynamic expectations that $NH_3$ ice should be present in Jupiter's upper cloud layer. We find a low intensity of this spectral feature, resulting probably from the rarity of the particle type, as well as from the inhomogeneity of the spatial distribution. Nonetheless, evidence that some Jovian aerosols are unambiguously composed of ammonia ice helps to validate the practice of modeling of broadband cloud opacity using larger ammonia particle sizes with compositionally indistinct extinction spectra. Additionally, although we lack the high spatial resolution of NIMS, and although we are probably sensitive to different $NH_3$ ice populations, we agree with the finding by Baines et al. (2002) that spectrally identifiable ammonia ice is nonuniformly distributed over the Jovian disk. Our modeling shows that the 10-μm $NH_3$ ice feature can be detected only when the ice aerosol is present at pressures of $\leqslant 500$ mbar, and the particle effective radius is within a factor of 2 of 1 μm. Since this altitude is higher than that of the equilibrium condensation level of ammonia near 750 mbar, detection of the 10-μm $NH_3$ ice feature at a particular location on Jupiter may be an indicator of convection, uplift, or recent cloud formation.

We utilize a dataset collected by the composite infrared spectrometer (CIRS) during the Cassini encounter with Jupiter in late 2000 and early 2001. The Jovian spectra presented here were obtained from focal planes 3 and 4 (FP3 and FP4), both $1 \times 10$ arrays of mid-IR detectors in the CIRS Fourier-transform spectrometer. FP3 spans the frequency range of 600–1100 $\text{cm}^{-1}$, covering the 1057-$\text{cm}^{-1}$ $NH_3$ ice absorption feature, and FP4 is sensitive to the 1100–1400 $\text{cm}^{-1}$ range. CIRS is more thoroughly described in Kunde et al. (1996), and Flasar et al. (2003) discuss preliminary results from the Jupiter flyby in 2000. Between 31 December 2000 and 11 January 2001, as Cassini was receding from Jupiter, CIRS obtained four global maps of the planet, with a spectral resolution of about 3 $\text{cm}^{-1}$. The low-latitude pixel resolution ranged from 2.5 to 5° of Jovian latitude/longitude, or 2500–6000 km, depending on distance between the spacecraft and the planet. We use data from the first global map, with the highest spatial resolution, to demonstrate the detection of the $NH_3$ ice $v_2$ absorption band.

Clapp and Miller (1993), in a study which seems to be the only reported measurement of the mid-infrared properties of $NH_3$ ice aerosols, observed a broadening of the 10-μm $v_2$ feature. The aerosol extinction shifted from a spectrum characteristic of a spherical particle to one characteristic of a prolate (cigar-shaped) spheroid, leading Clapp and Miller (1993) to speculate that initially spherical particles could be growing by coagulating into chains. We consider prolate spheroidal $NH_3$ ice particles in our synthetic spectra under the assumption that a similar method of aerosol growth may operate in Jupiter's atmosphere. Additionally, we find that prolate spheroidal particles with effective radii near 1 μm have advantageous properties for detection in Jupiter's atmosphere. Smaller (size parameter $x = 2\pi r/\lambda < 0.3$) Mie-scattering spheres are difficult to detect in Jupiter's spectrum because their peak extinction (at 1067 $\text{cm}^{-1}$) falls near the center of an $NH_3$ gas absorption band. Larger particles, with $x = 1.3$ or higher, have both excess absorption at lower frequencies, as well as a broadened extinction spectrum which makes their influence very difficult to distinguish from variations in gas or temperature profiles. We discuss these considerations in more detail in the spectral modeling section below.

Following these findings, we generated a suite of synthetic spectra using spherical as well as prolate spheroid $NH_3$ ice particles. We use a simple brightness temperature difference near the ice feature as a quantitative indicator of the presence of $NH_3$ ice in the CIRS data and find spatial variation of this brightness temperature difference on Jupiter. Using this indicator, we select two CIRS spectra for detailed comparisons with spectral models. We demonstrate detection of the $v_2$ absorption feature in an average spectrum obtained by co-adding individual CIRS spectra falling between 22–25°N and 140–240°W. We use planetographic coordinates for all CIRS observations. On the other hand, the $v_2$ ammonia ice absorption feature is not observed in a second average of CIRS spectra between 14–17°N and 10–70°W. This averaged spectrum is used to determine a model-dependent upper limit for the ammonia ice opacity there. Our modeling indicates that the 10-μm ammonia ice feature can be detected only when a significant quantity of particles with effective radii near 1 μm are located at pressures less than about 500 mbar. These restrictive criteria are the most likely reason that the 10-μm feature has eluded detection prior to this report.

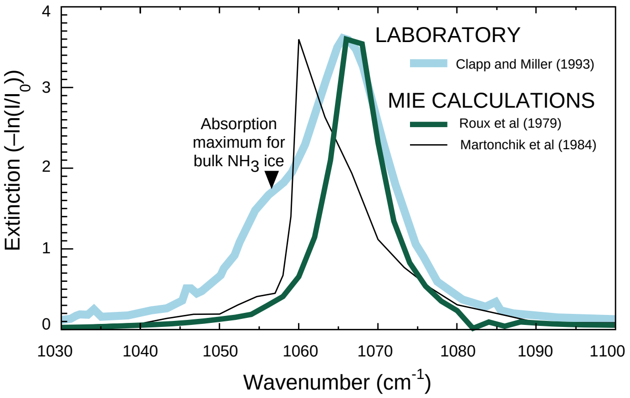

Fig. 1. Laboratory extinction curve for $NH_3$ aerosols measured by Clapp and Miller (1993), compared with scaled Mie extinction cross sections corresponding to two different sets of index of refraction data. Peak extinction for aerosols in the lab is shifted to higher frequencies, compared to the 1057 cm$^{-1}$ peak in imaginary index of refraction (black triangle). The frequency of the shifted peak favors the use of Roux et al. (1979) over Martonchik et al. (1984) index of refraction data.

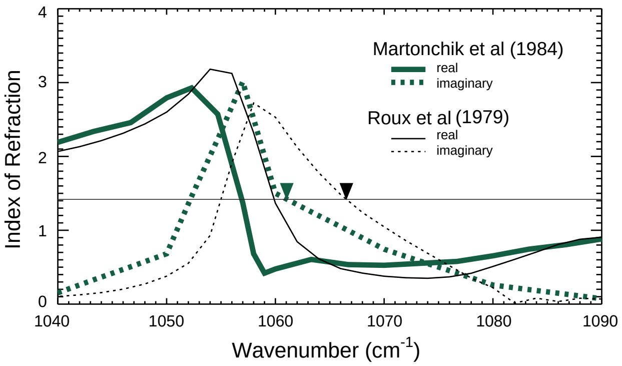

Fig. 2. Real (solid lines) and imaginary (dotted lines) index of refraction around the $NH_3$ ice $\upsilon_2$ band, from Martonchik et al. (1984; thick lines) and Roux et al. (1979; thin lines). For small particles the absorption peak shifts, from the location of the peak value of the imaginary index of refraction, to a frequency where the imaginary index of refraction is $\sqrt{2}$, and the real part of the index of refraction is low. Triangles indicate the locations of these shifted Fröhlich mode absorption peaks for each $NH_3$ index of refraction dataset.

## 2. Review: $NH_3$ ice aerosols in the laboratory

Understanding the interaction between infrared radiation and ammonia ice aerosols in Jupiter's atmosphere depends on several key parameters, including the shape, size distribution, and complex index of refraction of the ammonia ice particles. Observations of Jupiter cannot directly determine these parameters without relying on ground truth from laboratory measurements. Although laboratory studies of $NH_3$ ice condensation and optical properties in the 10-μm region are few, we summarize several crucial studies of ammonia ice here.

Ammonia aerosols were homogeneously nucleated in a cryogenic cell by Clapp and Miller (1993), who obtained particle extinction spectra over the frequency range of 700–4000 cm$^{-1}$. In Fig. 1, we show an extinction spectrum from the experiment of Clapp and Miller (1993), in which $NH_3$ aerosols were nucleated from a gas mixture of 2.5% $NH_3$ in helium, at a total pressure of 400 mbar and at a temperature of 111 K. The particles in this constant gas flow experiment had a residence time in the chamber of "several seconds," so they represent extremely fresh condensation products. Clapp (1995) retrieved particle size parameters for two sets of index of refraction data, assuming a log-normal particle distribution. For the Roux et al. (1979) dataset they found $r_{\text{med}} = 0.13$ μm and $\sigma = 0.70$ μm, and for Martonchik et al. (1984) they retrieved $r_{\text{med}} = 0.12$ μm and $\sigma = 0.62$ μm. We calculated extinction cross sections for these particles, and show them arbitrarily scaled for comparison in Fig. 1. The Roux et al. (1979) data more accurately match the frequency of the peak extinction of the aerosols created in the laboratory.

The black triangle in Fig. 1 indicates the frequency position of the peak of the bulk $NH_3$ absorption (i.e., the peak of the imaginary index of refraction). The shift of the particle absorption to higher frequencies, as shown in Fig. 1, is described by Clapp (1995) and references therein as a Fröhlich, or surface, mode. For particles with small size parameters, the electric field of the incident radiation is roughly uniform, inducing all the molecules in the particle to vibrate in phase. This creates a net dipole moment for the particle and shifts the absorption band to higher frequencies. The Fröhlich mode exists only for small size parameter particles, is strongly dependent on shape, and occurs only when the imaginary index of refraction is equal to $\sqrt{2}$ and the real index of refraction is small. Fig. 2 compares real and imaginary index of refraction data near the $\upsilon_2$ band, for the Martonchik et al. (1984) and Roux et al. (1979) datasets. The black triangles in Fig. 2 indicate frequencies where the Fröhlich mode conditions are met. Based on the better agreement between the Clapp and Miller (1993) laboratory spectrum and the Roux et al. (1979) calculation, we select the Roux et al. (1979) index of refraction dataset for use in our own calculations to be discussed below.

Clapp and Miller (1993) also studied the evolution of the aerosol extinction spectrum over time. In Fig. 3, we compare their laboratory-derived $NH_3$ aerosol extinction spectrum with a calculated extinction spectrum for 0.13-μm spheres, scaled to match the spectrum near the $\upsilon_3$ band near 3 μm (not shown). Scaling is required because the experiment measures attenuation of an infrared source, while Mie calculations yield particle cross sections in units of area. The observed spectrum in Fig. 3 was obtained by Clapp and Miller after 4 minutes of stagnant conditions, whereas the extinction spectrum in Fig. 1 corresponds to particles in the first several seconds of their formation. The evolution of the aerosol extinction spectrum is consistent with a change in particle size or shape, since small spheres were effective at fitting the shorter-timescale extinction spectrum of Fig. 1. Clapp and Miller (1993) state that a much larger sphere

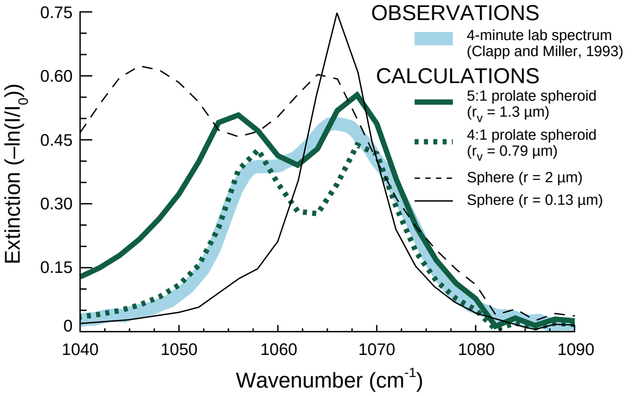

Fig. 3. The extinction of $NH_3$ aerosols after 4 min, as measured by Clapp and Miller (1993), is compared with particle extinction cross-section calculations. The extinction spectrum for 0.13-μm spheres was scaled by Clapp and Miller (1993) to agree with extinction at 3 μm (not shown), while the other curves have been arbitrarily scaled to fit within the plot region. The 0.13-μm sphere spectrum was calculated with a log normal size distribution with $\sigma = 0.70$ μm. The other spectra were calculated with monodisperse (single-sized) particle size distributions.

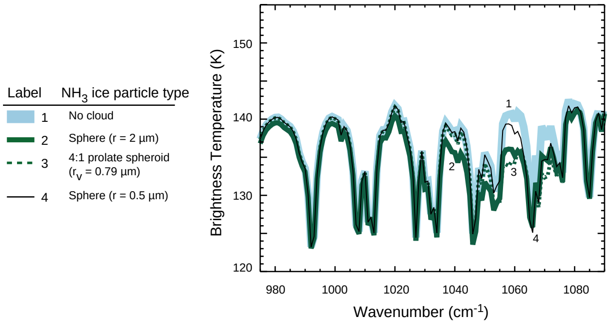

Fig. 4. Synthetic Jovian spectra for three particle types, as described in the legend. All three simulated clouds are distributed with a particle-to-gas scale height ratio of 1, with the cloud confined between 100 and 680 mbar. The total optical depth for each cloud, defined at the frequency of maximum extinction, is 1. The largest value of $\alpha = T_{1040} - T_{1060}$ is associated with the particle nearest 1 μm in size (particle 3; $\alpha = 3.3$), with smaller (particle 4; $\alpha = 0.1$) and larger (particle 2; $\alpha = 1.0$) sizes having a diminished effect on α. The cloud-free case has $\alpha = -1.3$.

would exhibit the broadening of the 4-minute spectrum at 9.5 μm, but a large sphere would produce non-resonant scattering features at 3 μm, which they did not observe. Instead, Clapp and Miller suggested coagulation of small aerosols into chain-like particles to describe the spectral evolution. We show normalized extinction curves for two randomly-oriented prolate spheroid particle distributions in Fig. 3: a prolate spheroid with $r_v = 1.3$ μm (where the volume-equivalent radius $r_v$ is the radius of a sphere that has the same volume as the spheroid) and a major-to-minor axis ratio of 5:1, as well as a 4:1 prolate spheroid with $r_v = 0.79$ μm. Unless otherwise noted, calculated extinction curves are for monodisperse size distributions. Since the 4:1 prolate spheroid provides a good match to the shape of the laboratory aerosol extinction spectrum, we use this type of $NH_3$ ice particle in our model spectra below.

Pope et al. (1992) measured scattering phase functions, at visible wavelengths, of $NH_3$ aerosols generated in the laboratory, and found a good match between 0.5-μm particle phase functions and Jovian phase functions reported by Smith and Tomasko (1984). In the 10-μm region, 0.5-μm particles are well modeled as Mie-scattering spheres, and we examine this particle type as well. Pope et al. (1992) also reported that their laboratory data required a mixture of particle shapes.

## 3. Spectral modeling

In order to calculate optical properties of non-spherical ammonia ice particles, we used a FORTRAN implementation (Mishchenko and Travis, 1998) of the T-matrix algorithm described by Wielaard et al. (1997). Originally developed by Waterman (1971), this method allows absorption cross sections, scattering cross sections, and scattering phase function expansion coefficients to be derived from a transition matrix (or T-matrix). In the T-matrix algorithm, the incident, scattered, and internal electromagnetic fields are expanded as vector spherical functions, and a numerical solution of Maxwell's equations produces the T-matrix, which relates the scattered and incident field expansion coefficients. The frequency-dependent particle scattering properties are then used as inputs for our Jovian radiative transfer code, a correlated-k approach (Lacis and Oinas, 1991) in a multi-stream discrete ordinates model (Goody and Yung, 1989). Synthetic spectra were found to be in good agreement with a full line-by-line calculation (Kunde and Maguire, 1974). We use the HITRAN 1996 line atlas to model contributions from $CH_4$, $NH_3$, $PH_3$, $C_2H_2$, and $CH_3D$, and we also include pressure-induced hydrogen absorption.

Across the 600–1125 $cm^{-1}$ range of CIRS focal plane 3, spectral information from vertical profiles of aerosol, ammonia gas, phosphine gas, and temperature are intermingled. For particular particle types, the difference in brightness temperature between the 1040 $cm^{-1}$ and 1060 $cm^{-1}$ continuum peaks is strongly affected by the ammonia ice feature (see Fig. 4). We define a brightness temperature difference α, where

$$\alpha = T_{1040} - T_{1060}, \tag{1}$$

and the brightness temperatures $T_{1040}$ and $T_{1060}$ are defined simply as the peak brightness temperatures within the respective spectral windows defined by $NH_3$ gas absorption of $[1033, 1046]$ $cm^{-1}$ and $[1053, 1065]$ $cm^{-1}$. Although vertical profiles of temperature, ammonia gas, and phosphine gas are influential in this spectral window, their effect on α is minimal. Figs. 5–7 demonstrate the spectral influence of temperature, ammonia gas, and phosphine gas profiles, and we discuss each factor in turn below. Our choice of α as an indicator of $NH_3$ ice in the spectrum is based on two main

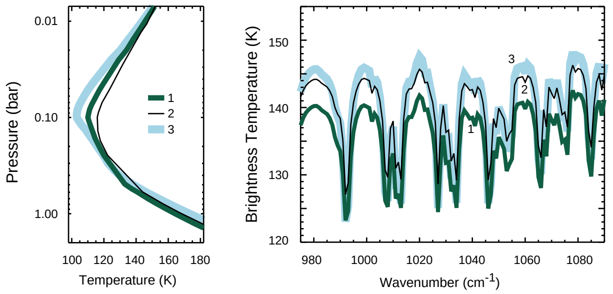

Fig. 5. Three temperature profiles are shown, along with their effects on the synthetic Jovian spectrum. Brightness temperature difference $\alpha = -1.3$ for profile 1, $\alpha = -1.2$ for profile 2, and $\alpha = -1.4$ for profile 3.

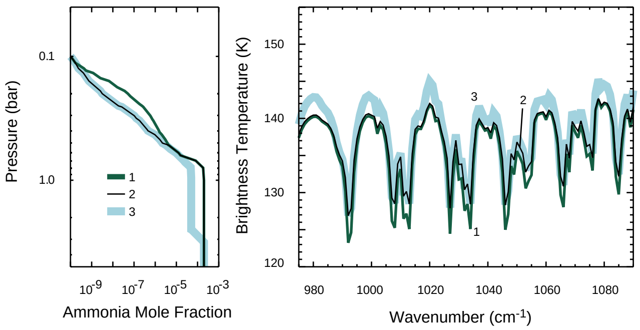

Fig. 6. Three $NH_3$ mole fraction profiles are shown, along with their effects on the synthetic Jovian spectrum. Brightness temperature difference $\alpha = -1.3$ for profile 1, $\alpha = -1.2$ for profile 2, and $\alpha = -1.4$ for profile 3.

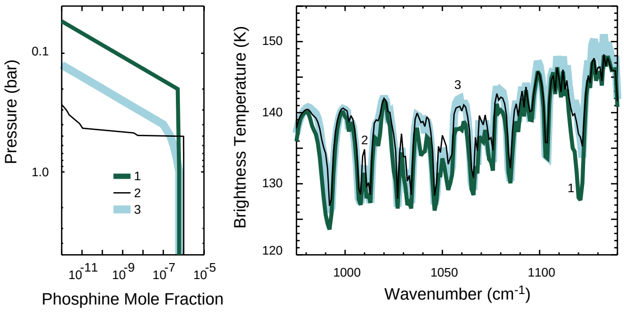

Fig. 7. Three $PH_3$ mole fraction profiles are shown, along with their effects on the synthetic Jovian spectrum. Brightness temperature difference $\alpha = -0.9$ for profile 1, $\alpha = -1.2$ for profile 2, and $\alpha = -2.4$ for profile 3.

considerations: it is easy to compute, and its small spectral width makes a strong argument for a definitive compositional identification.

Example spectra for three $NH_3$ ice particle types are compared with a cloud-free model spectrum in Fig. 4. The smallest particle (number 4) has a normalized extinction spectrum that is almost identical to that of the 0.13-μm sphere shown in Fig. 3. The peak extinction near 1065 cm$^{-1}$ coincides with the center of an ammonia gas absorption band, hiding the $NH_3$ ice spectral signature. The effect of these particles on the 1060 cm$^{-1}$ brightness temperature is minimal, so the effect on the brightness temperature difference $\alpha$ is also minimal. Thus, although 0.5-μm particles may be suggested for Jupiter at other wavelengths (Pope et al., 1992), we do not expect the small particles to be detectable at 10 μm. The next larger particle shown is a prolate spheroid with $r_v = 0.79$ μm (number 3 in Fig. 4), a size chosen because it is analogous to a chain of four 0.5-μm particles. Particle 3 is much more effective than particle 4 at depressing the continuum level at 1060 cm$^{-1}$, primarily as a result of its larger size. The depressed brightness temperature at 1070 cm$^{-1}$ is a shape effect, due to the "twin peaks" in the extinction spectrum of this prolate spheroid (see Fig. 3). Particle 3 also has virtually no effect on the spectrum at 1040 cm$^{-1}$, so it has ideal qualities for being detected via the brightness temperature difference $\alpha$. Finally, particle 2 shows that for large enough particles, the effect on the spectrum at 1040 cm$^{-1}$ and at 1060 cm$^{-1}$ is similar. Not only does the simultaneous depression of the 1040 and 1060 cm$^{-1}$ continuum peaks disable the use of $\alpha$ as a detector of $NH_3$ ice, but it also mimics other spectral effects such as that of phosphine, as will be discussed below. These results indicate that only particles with sizes within a factor of 2 from 1 μm can be detected using the brightness temperature difference $\alpha$.

Fig. 5 shows the effect of the temperature profile on synthetic Jovian spectra. In the cores of the $NH_3$ absorption bands, the spectrum is more sensitive to the temperature near 400 mbar, so spectrum 2 has the highest brightness temperatures there. The intervening continuum regions reach unit optical depth at pressures near 600 mbar, so spectrum 3 has the highest brightness temperatures there. Note that for all sample temperature profiles, $T_{1040}$ and $T_{1060}$ scale together, so that there is little effect on $\alpha$. The effect of $NH_3$ distribution on the spectrum, as seen in Fig. 6, is similar to the temperature effect. The 23.5°N CIRS spectrum presented later is modeled using temperature and ammonia profiles marked 1, and the 15.5°N CIRS spectrum presented later uses temperature and ammonia profiles marked 2. Ammonia profile 3, which has an ammonia depletion below the condensation level as suggested by radio measurements (de Pater et al., 2001), did not fit either of our sample CIRS spectra. Although the temperature and ammonia vertical profiles produce similar effects on the Jovian spectrum in the 975–1090 cm$^{-1}$ interval, we can disentangle the two components when fitting CIRS spectra by first using the wing of the S(1) line of $H_2$ to constrain the temperature profile and then selecting an $NH_3$ profile that provides a good fit in the 975–1090 cm$^{-1}$ interval.

Spectral sensitivity to phosphine is shown in Fig. 7. Profile 1 was derived by Edgington et al. (1998) to fit an HST ultraviolet spectrum taken at 6°N, but they regard this profile as an upper limit to the amount of phosphine in the upper troposphere, since they did not include aerosols in their modeling. Profile 3 is the predicted photochemical distribution at 6°N of phosphine from Edgington et al. (1998), and profile 2 is our best fit to the example CIRS spectra

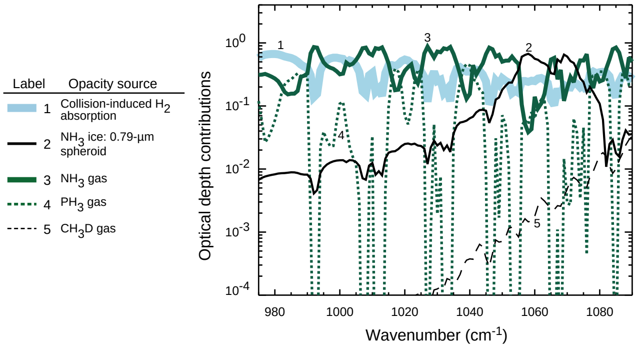

Fig. 8. For five opacity sources (see legend), the fractional contribution to the total optical depth, calculated at the level of $\tau = 1$, is shown as a function of wavenumber. The shape of the curve for each opacity source is a function of (1) the spectral properties of the opacity source itself and (2) the spectral properties of any stronger opacity sources that dominate it. The ammonia ice cloud in this case has a total optical depth of 1 and is composed of 4:1 prolate spheroids with $r_v = 0.79$ µm. The aerosol profile used is the "extended" distribution shown in Fig. 10. Ammonia ice (curve 2) is the dominant opacity source at 1060 and 1070 $cm^{-1}$, but has little influence elsewhere.

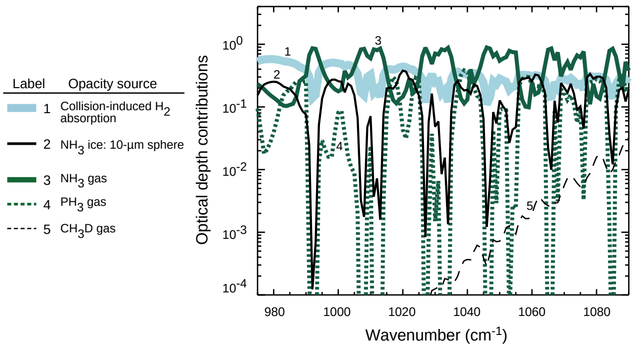

Fig. 9. Fractional optical depths, as in Fig. 8. In this case, the ice cloud is composed of 10-µm spheres, and the aerosol profile used is the "compact" distribution shown in Fig. 10, with a total cloud optical depth of 5. Due to the large particle size, ammonia ice (curve 2) is essentially grey: it has strong effects in each of the continuum regions sandwiched between ammonia gas band centers (peaks in curve 3).

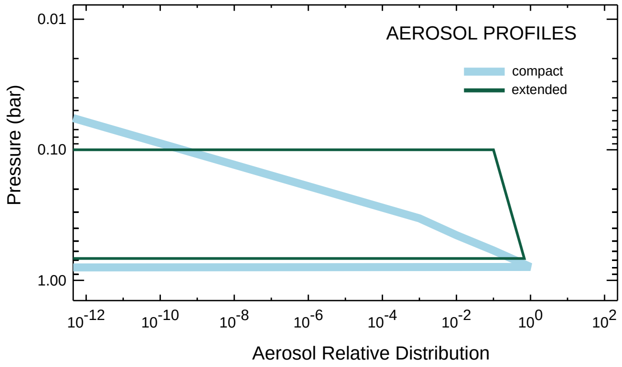

Fig. 10. Two aerosol vertical distributions were tested in this study. The compact distribution has a cloud base of 790 mbar and a particle-to-gas scale height ratio $H_p/H_g$ of about 1/8. The aerosol density in this distribution is also proportional to the maximum cloud density calculated by a thermochemical equilibrium condensation model (Weidenschilling and Lewis, 1973; Atreya et al., 1999). The extended distribution has $H_p/H_g = 1$, with cloud particles confined between pressures of 680 and 100 mbar.

to be shown later. To obtain our best fit, we took profiles with constant $PH_3$ mole fractions up to a cutoff level, and allowed the deep mole fraction and the cutoff level to vary. However, the similarity between the spectra generated using our best fit profile and the Edgington et al. (1998) photochemical profile shows that our ability to constrain the phosphine profile is limited. For large amounts of phosphine at pressures less than 500 mbar, there is noticeable suppression of the brightness temperature at 1060 $cm^{-1}$, where we hoped to detect the influence of $NH_3$ ice. However, since the 1040 $cm^{-1}$ continuum peak is depressed as well, the brightness temperature $\alpha$ is not strongly affected. Enhanced $PH_3$ also results in an intensification of the $PH_3$ $\upsilon_4$ band feature centered at 1118 $cm^{-1}$, but we found virtually no correlation between $\alpha$ and the strength of the 1120-$cm^{-1}$ $PH_3$ feature in a set of zonally averaged CIRS spectra ranging from 30°S to 30°N.

Figs. 8 and 9 show the relative contributions to the total opacity from $NH_3$, $PH_3$, and $CH_3D$ gas, $NH_3$ ice, and collision-induced $H_2$ absorption. At each frequency, the fractional optical depth of each opacity source is plotted, for the altitude where the total optical depth is unity. Gas and temperature profiles are the same for both cases, but the $NH_3$ ice cloud (curve 2) in Fig. 8 is composed of 0.79-µm 4:1 prolate spheroids (particle 3 in Fig. 4), and the cloud in Fig. 9 is composed of 10-µm $NH_3$ ice spheres. For the 0.79-µm particle cloud, the total cloud optical depth was unity (at the frequency of maximum extinction, 1068 $cm^{-1}$ for this particle type), and the aerosols were distributed between 680 and 100 mbar with a particle-to-gas scale height ratio $H_p/H_g = 1$ ("extended" aerosol profile in Fig. 10). For the 10-µm particle cloud, the peak optical depth was 5, and the "compact" aerosol profile (Fig. 10) was used, with a cloud base at 790 mbar and $H_p/H_g = 1/8$. The strong absorption at 1060 $cm^{-1}$ is apparent for the small spheroids in Fig. 8, whereas for the large aerosols in Fig. 9, aerosol opacity is high in all the continuum regions between the $NH_3$ band centers (i.e., between all the peaks in curve 3).

For one preliminary set of 1000 synthetic test spectra, with a wide range of gas and temperature profiles, $\alpha$ ranged from −3.7 to −1.8 K for cloud-free models and from −3.3 K to 7.9 K for $NH_3$ ice cloud models with a cloud optical depth of 2 and the extended aerosol distribution of Fig. 10. In this set of synthetic spectra, three particle types were tested: 0.5-µm spheres, and 5:1 prolate spheroids with volume-effective radii of 0.85 and 2.6 µm. All synthetic spectra with values of $\alpha > 2$ had the 0.85-µm prolate spheroids $NH_3$ ice particles. This follows from our conclusion that only particles in the 1-µm size range are detectable using $\alpha$ as an indicator. Spectra in this set with very high values of $\alpha > 5$ had the

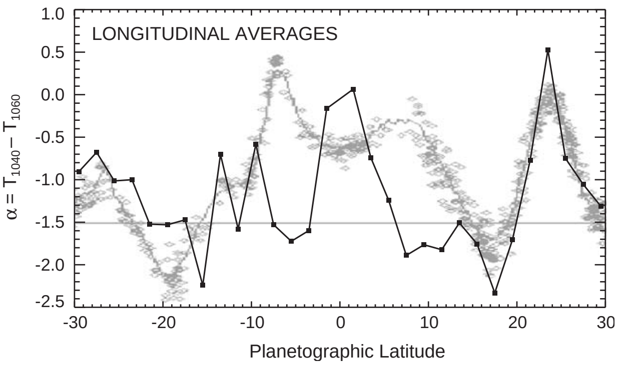

Fig. 11. Brightness temperature difference α as a function of latitude. Each point is calculated for a spectrum averaged over all longitudes, 3° wide in latitude. Spectral averaging bins overlap their neighbors to the north and south by 1°. For comparison, the HST-derived zonal wind profile of García-Melendo and Sánchez-Lavega (2001) is shown in grey, with a maximum eastward speed of 154 m $s^{-1}$ and a zero point indicated by the horizontal line.

additional requirement of reduced $NH_3$ in the 600–800 mbar region. The 600–800 mbar $NH_3$ mole fraction affects α in these cases because the reduced gas opacity means that a larger fraction of the total opacity at 1060 $cm^{-1}$ is provided by the ammonia ice cloud.

## 4. Observations

Using the low-latitude portion of a CIRS global map of Jupiter (described in the Introduction), we first search for spatial variation in the ammonia ice signature by obtaining zonally averaged $\alpha = T_{1040} - T_{1060}$. Latitudinal structure is clearly evident in the plot of α as a function of latitude (Fig. 11). Each point marks a value of α calculated from a spectral average over all data falling within a band 3° wide in latitude. There is a 1° overlap to the north and south of each point in Fig. 11. For example, one point represents the 0°–3°N band, and the next represents the 2°–5°N band. The number of pixel footprints per bin ranged from 176 to 245. Particularly high values of α, indicating detection of the $v_2$ $NH_3$ ice feature, occur near 23°N and near the equator. Studies of synthetic spectra indicate a small variation of α due to emission angle, with an increase of up to 0.3 K from 0° to 30°, where the magnitude of the variation depends on the model atmosphere assumed. Since Cassini was within a degree of the equatorial plane, this increase in α is monotonic from equator to pole and could not account for the latitudinal variation seen in Fig. 11. The overlaid zonal wind profile is an average of 3 years of HST data from García-Melendo and Sánchez-Lavega (2001), with a maximum eastward speed of 154 m $s^{-1}$ and a zero point indicated by the horizontal line. The zonal wind profile will be discussed later in the context of the dynamical implications of the latitudinal variation in the ammonia ice spectral feature.

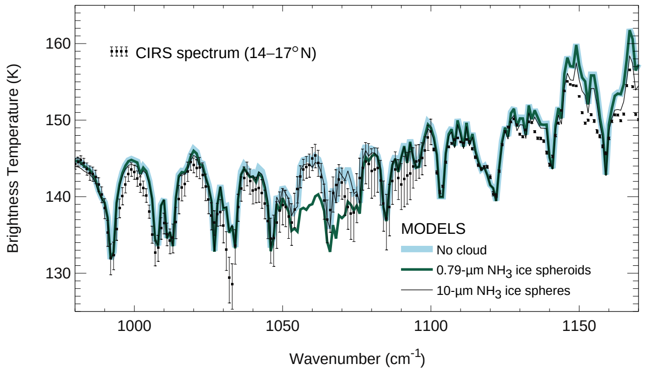

Fig. 12. CIRS spectrum (14–17°N, 10–70°W) co-added from 46 FP3 spectra ($v < 1100$ $cm^{-1}$) and 44 FP4 spectra ($v > 1100$ $cm^{-1}$). CIRS FP4 has greater sensitivity than FP3, so the FP4 error bars are barely visible. Synthetic spectra were all generated with temperature profile 2 (Fig. 5), $NH_3$ profile 2 (Fig. 6), and $PH_3$ profile 2 (Fig. 7). The observed spectrum near 1060 $cm^{-1}$ shows no evidence of the $NH_3$ ice feature. At frequencies greater than 1125 $cm^{-1}$, a grey cloud improves the fit to the observations. Grey cloud particles were well modeled as large ($r = 10$ µm) ammonia ice spheres, with a total cloud optical depth of 2 and the "compact" aerosol distribution of Fig. 10. For the $NH_3$ ice spheroid case, cloud particles were modeled as 0.79-µm randomly oriented 4:1 prolate spheroids, with a total cloud optical depth of 1 and the "extended" aerosol distribution of Fig. 10.

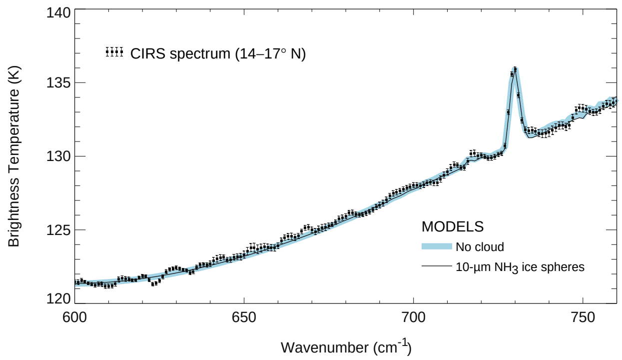

Fig. 13. Observations and models as described in Fig. 12, but for the low-frequency portion of CIRS FP3. This spectral region is dominated by the hydrogen S(1) line and almost exclusively shaped by the 50–700 mbar temperature profile, except for the stratospheric acetylene line seen in emission at 730 $cm^{-1}$.

Spectra showing no evidence of $NH_3$ ice at 1060 $cm^{-1}$ are characterized by low values of α (less than about −1.5 K). The non-detection of $NH_3$ ice at 10 µm by Shaffer et al. (1985) from Voyager 1 IRIS measurements of the North Tropical Zone may possibly be due to the spatial variation indicated by Fig. 11, or due to temporal variation. Since α is low from 6° to 20°N, we looked to that region to find a sample $NH_3$ ice-free spectrum. The CIRS spectrum shown in Fig. 12 is an average of 46 FP3 spectra and 44 FP4 spectra falling within 14–17°N and 10–70°W. All fits shown use the same vertical distributions of temperature, $NH_3$ gas, and $PH_3$ gas, where we derive the temperature profile from the S(1) line between 600 $cm^{-1}$ and about 750 $cm^{-1}$ (see Fig. 13).

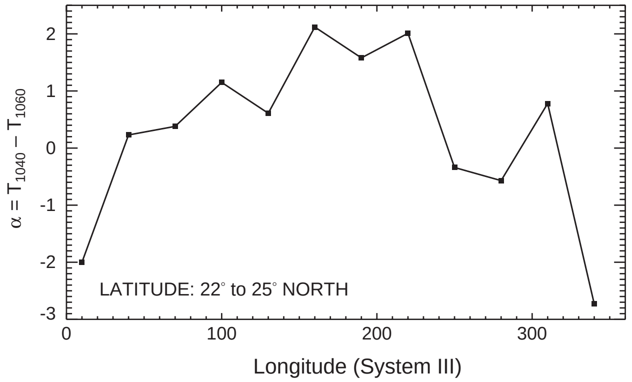

Fig. 14. Brightness temperature difference $\alpha$ calculated for a latitude band between 22° and 25°N, with bins 40° wide in longitude, overlapping 10° on each side.

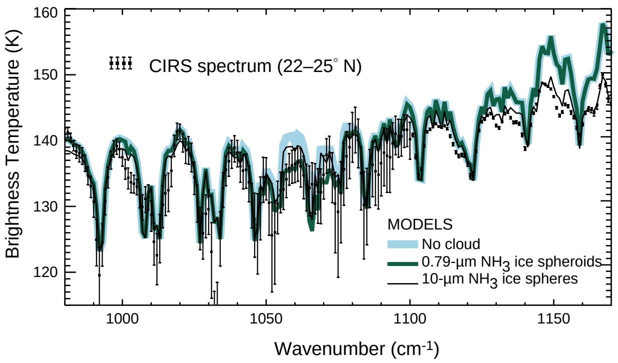

Fig. 15. CIRS spectrum (22–25°N, 140–240°W) co-added from 46 FP3 spectra ($v < 1100$ cm$^{-1}$) and 50 FP4 spectra ($v > 1100$ cm$^{-1}$). CIRS FP4 has greater sensitivity than FP3, so the FP4 error bars are barely visible. Synthetic spectra were all generated with temperature profile 1 (Fig. 5), $NH_3$ profile 1 (Fig. 6), and $PH_3$ profile 2 (Fig. 7). The $NH_3$ ice feature can be seen in the observed spectrum near 1060 cm$^{-1}$. Two particle sizes are required to fit the spectrum: small (near 1 µm) particles to fit the 1060 cm$^{-1}$ $NH_3$ ice feature, and large (10 µm) particles to fit the spectrum at frequencies greater than 1125 cm$^{-1}$. The smaller particles were modeled as 0.79-µm randomly oriented 4:1 prolate spheroids, with a total cloud optical depth of 0.75 and the extended aerosol distribution of Fig. 10. The larger particles were well modeled as 10-µm ammonia ice spheres, with a total cloud optical depth of 5 and the compact aerosol distribution.

The CIRS spectrum in Fig. 12 is compared with two $NH_3$ ice cloud spectra: one with 10-µm spheres and one with prolate spheroids with effective radii near 1 µm (see figure caption). The 1-µm particle spectrum produces a noticeable $NH_3$ ice feature at 1060 cm$^{-1}$ and gives a poor fit to the CIRS data in that spectral region, which has a value of $\alpha = -2.3$. Away from the vicinity of 1060 cm$^{-1}$, the $NH_3$ ice cloud spectrum is indistinguishable from the clear sky spectrum. For smaller $NH_3$ ice optical depths ($\tau < 0.2$), the spectrum matches the CIRS spectrum to within the noise level. For these aerosol parameters, the $\tau < 0.2$ condition translates to a column density detection limit of on the order of less than $2.5 \times 10^6$ cm$^{-2}$ above the 625 mbar level. The essentially grey cloud modeled using large ($r = 10$ µm) Mie-scattering ammonia ice spheres has a minimal effect at frequencies less than 1125 cm$^{-1}$, since those frequencies do not probe the deeper layers where most of the aerosol opacity is found for the "compact" aerosol profile (Fig. 10). In the absence of aerosol opacity, frequencies from 1125 to 1200 cm$^{-1}$ can sense to pressures of slightly more than 800 mbar, so the discrepancy between the CIRS data and the clear sky model spectrum in this region requires aerosol opacity at the pressure levels near the canonical thermodynamic equilibrium cloud base for 2–3 × solar ammonia (Weidenschilling and Lewis, 1973; Atreya et al., 1999). Due to the depth of this cloud layer, even if the cloud contained spectrally identifiable ammonia ice, the spectrum at 1060 cm$^{-1}$ would be sensitive to altitude levels higher than the cloud, and thus the $NH_3$ ice feature would go undetected.

The zonal maximum in $\alpha$ occurs at the 3-degree band centered on 23.5°N (Fig. 11), so we selected that latitude as a candidate latitude to prospect for $NH_3$ ice. In Fig. 14, we show $\alpha$ as a function of System III longitude, in the 3° band from 22 to 25°N. Each point is calculated from an average spectrum using all FP3 pixel footprints falling within a 40°-wide bin, with 10° overlap between bins to the east and west. The number of spectra per bin ranged from 12 to 28. A very strong longitudinal effect is seen in Fig. 14, with the peak values of $\alpha$ falling between 140° and 240°W longitude. The amplitude of this curve is $5K$, somewhat larger than the $3K$ amplitude of the zonally averaged $\alpha$ curve in Fig. 11. Part of this amplitude is the greater noise level in the brightness temperatures used to construct Fig. 14, since the sample size for each point is much smaller. However, it is likely that some of the reduction in amplitude, going from the longitudinal scan in Fig. 14 to the zonal averages of Fig. 11, is a result of spatial averaging of inhomogeneous cloud properties. Further detailed studies of the spatial variation of the $NH_3$ ice signature should be done to quantify the uncertainty and determine the maximum amount of spatial information content on the variation of the ice feature in the CIRS observations.

In Fig. 15, the observed spectrum is an average of 46 FP3 pixels and 50 FP4 pixels falling in the region between 22–25°N and 140–240°W. This location was chosen to isolate the highest values of $\alpha$ (see Fig. 14), and the spectrum shown has $\alpha = 2.2$. The synthetic spectra have gas and temperature vertical distributions that match the FP3 data in both the $NH_3$ ice $v_2$ region (Fig. 15), as well as the portion of the hydrogen S(1) line from 600 to about 750 cm$^{-1}$ (not pictured). For the clear sky model, the CIRS 1060 cm$^{-1}$ brightness temperature is overestimated. The observed spectrum near 1060 cm$^{-1}$ is fitted by an ammonia ice cloud model using 4:1 prolate spheroids with volume-equivalent radius $r_v = 0.79$ µm. For comparison with the spectra shown in Fig. 15, Fig. 16 shows the frequency-dependent pressure level where unit optical depth is reached for each model atmosphere case.

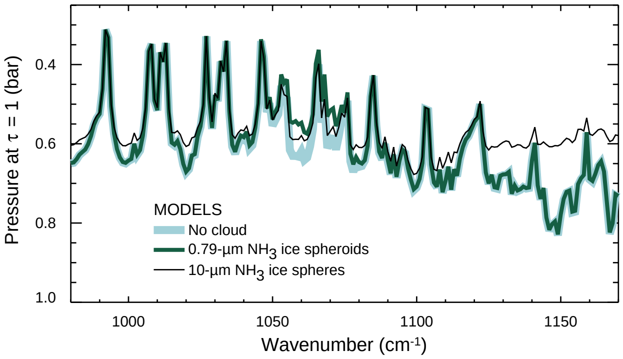

Fig. 16. For the model spectra in Fig. 15, this plot shows the frequency dependent pressure level at which the total atmospheric optical depth is 1.

The synthetic spectrum with the $NH_3$ ice spheroid cloud with $\tau = 0.75$ in Fig. 15 gives the best fit to the observed 23.5°N spectrum in the 1060 $cm^{-1}$ region. A cloud with the same particle parameters and relative vertical distribution, but with a larger maximum optical depth of 2, underestimates the 1060 $cm^{-1}$ brightness temperature but still falls within the noise level. However for $\tau > 2$, the synthetic brightness temperature is too low to agree with the CIRS observations, just as the clear sky model in Fig. 15 is a poor fit because it exceeds the 1-$\sigma$ noise level at 1060 $cm^{-1}$. Using these constraints on the spectrally identifiable ammonia ice atmospheric optical depth, we estimate the aerosol column density above the pressure level where the atmospheric optical depth reaches unity, finding a maximum column density of $2\times10^7$ particles $cm^{-2}$ above the 400 mbar level, and a minimum column density of on the order of $3\times10^6$ particles $cm^{-2}$ above the 600 mbar level, assuming a particle type of 0.79-μm 4:1 prolate $NH_3$ ice spheroids. Particles with sizes around 2 μm or larger would not fit the data well due to additional absorption at 1040 $cm^{-1}$. Smaller particles would have too strong absorption near 1067 $cm^{-1}$ and too weak absorption at 1060 $cm^{-1}$, similar to spectrum number 4 in Fig. 4. The 23.5°N CIRS spectrum, as was the case for the 15.5°N spectrum, requires grey aerosol opacity to match the spectrum between 1125 and 1200 $cm^{-1}$. The two clouds required to match both the 1060 $cm^{-1}$ region and the 1125 –1200 $cm^{-1}$ region are distinct in both extinction spectrum and vertical distribution, but there is no reason for the existence of one to exclude the other. Thus, our best fit to the observed spectrum has a two-component cloud, with spectrally identifiable ammonia ice following the "extended" aerosol profile ($H_p/H_g = 1$; see Fig. 10), in addition to a grey cloud concentrated deeper, following the "compact" aerosol profile ($H_p/H_g = 1/8$). Since the observed spectrum requires not only different particle types but also different scale heights for the two portions of the spectrum with frequencies less than or greater than 1100 $cm^{-1}$, it follows that two distinct cloud types are being detected. Higher spatial resolution observations would be needed to determine whether the two cloud types are spatially distinct or spatially coincident.

## Discussion

Arguing that the $v_2$ absorption band of $NH_3$ ice can best be identified in Jupiter's spectrum by a depression of the thermal radiation at 1060 $cm^{-1}$, we define the brightness temperature difference $\alpha = T_{1040} - T_{1060}$ as an indicator of the ice feature. Modeled particle extinction spectra (Figs. 3 and 4) show that particles smaller or larger (by about a factor of 2) than 1 μm in effective radius have a much weaker effect on $\alpha$ and thus are poorly detected using this parameter. In addition to the particle size constraint, spectral modeling shows that any 1-μm particles present deeper than about 500 mbar will be too far below the level of the peak contribution to the 1060 $cm^{-1}$ intensity to be detected. Our 23.5°N spectrum requires at least two types of cloud particles. The ammonia ice feature at 1060 $cm^{-1}$ requires ∼ 1-μm particles in an extended cloud with $H_p/H_g = 1$ (see Fig. 16), while the spectrum from 1125 to 1200 $cm^{-1}$ can be matched by a more compact grey cloud with $H_p/H_g = 1/8$ and an optical depth of 5. We can effectively model the grey cloud using 10-μm $NH_3$ ice spheres, but since this cloud lacks sharp spectral features, it is difficult to conclusively identify its composition. Our 15.5°N spectrum shows no evidence of the extended cloud of 1-μm ammonia ice particles, but still requires a compact cloud of 10-μm ammonia ice particles with an optical depth of 2.

A large particle cloud has also been invoked to provide the necessary opacity in the thermal infrared data of Voyager IRIS (Marten et al., 1981; Shaffer et al., 1986) and ISO-SWS (Brooke et al., 1998). Orton et al. (1982) also found a compact cloud of large ($r > 3$–10 μm) particles through analysis of thermal infrared data, drawing a similar conclusion to Marten et al. (1981) that the lack of ammonia ice spectral features ruled out small particles. The fact that the feature is seen in our higher spatial resolution spectra, but not in less resolved observations, is a strong argument for the spatial inhomogeneity of the class of particles capable of producing the ammonia ice signature. Smaller particles have been suggested by West et al. (1986); ∼ 1−μm particles) and Pope et al. (1992; 0.5-μm particles) to match the Pioneer photopolarimetry analysis of Smith and Tomasko (1984) at visible wavelengths.

Spatially resolved $NH_3$ ice clouds were mapped from anomalously low NIMS reflectance in the 2.74-μm channel by Baines et al. (2002). Comparing their maximum reflectance anomalies with the 2.7-μm reflectance of the ISO spectrum (Brooke et al., 1998) led Baines et al. (2002) to conclude that their particle sizes and/or cloud optical depths needed to be perhaps a factor of 3 larger than those retrieved from the ISO spectrum ($r$=10 μm). Thus it is unlikely that the same clouds seen by Baines et al. (2002) would produce an identifiable ammonia ice feature in the CIRS spectrum at 1060 $cm^{-1}$. Baines et al. (2002) found that their ammonia ice clouds are correlated with regions of dramatic vertical uplift in the wake of the Great Red Spot (near 10°S) and to the east of 5-μm hotspots in the North Equatorial Belt (at 2–7°N). To investigate the correlation between uplift and the 10-μm ammonia ice feature, we compare the plot of zonally averaged $\alpha$ with the zonal wind profile of García-Melendo and Sánchez-Lavega (2001) in Fig. 11. Upwelling has traditionally been expected in regions of anticyclonic flow, where eastward winds increase poleward. Colder tropopause temperatures observed in anticyclonic zones can be attributed to adiabatic cooling associated with uplift (e.g., Flasar, 1986). Thus, one would expect vertical motions at equatorial latitudes to be upward, and the higher value of $\alpha$ there is consistent with this. The coincidence of a local maximum in $\alpha$ in the core of the eastward jet at 23°N, however, is puzzling, because it is just north of an anticyclonic region. Retrievals of the $NH_3$ gas abundances and relative humidities from CIRS spectra by Achterberg et al. (2003) indicate that the highest values occur in anticyclonic flow, at least at low latitudes. In particular, high relative humidities and abundances are observed at the equator and just south of the 23°N jet maximum. The reason for the relative offset near 23°N of the gas abundance and relative humidity from the 10-μm ice feature is not immediately apparent, and will require further study. Since the magnitude of the latitude offset is only the size of one averaging bin width (3° in latitude), the discrepancy may partly be an artifact of our spatial averaging method.

Although some moderately high values of $\alpha$ are seen at the latitudes of the main spectrally identifiable ammonia ice clouds of Baines et al. (2002), higher spatial resolution would be required to make a definitive comparison with the discrete and inhomogeneous clouds detected by NIMS reflectance maps at 3 μm. Our strongest zonally averaged 10-μm ammonia ice signature at 23.5°N does not seem to correspond to any identifiable ammonia ice clouds at 3 μm, although it should be noted that more than 4 years separate the two datasets, and the influence of temporal variation could be quite significant. Some of the North Equatorial Belt clouds identified by Baines et al. (2002) and associated with 5-μm hotspots fall within the peak of $\alpha$ at the equator in Fig. 11. Determining longitudinal variation of the ice signature may be within the limits of sensitivity of the CIRS Jupiter measurements, but more work must be done to constrain measurement uncertainty. In addition, three other maps of Jupiter (unused in this study) were made in the two weeks after Cassini–Jupiter closest approach, and these datasets may also help to constrain spatial and temporal variation of the 10-μm ice feature.

## Acknowledgements

We wish to thank Richard K. Achterberg for very helpful discussions. This work was performed while the lead author held a National Research Council Research Associateship Award at NASA Goddard Space Flight Center.

## References

Achterberg, R.K., Conrath, B.J., Gierasch, P.J., Simon-Miller, A.A., Flasar, F.M., 2003. Cassini CIRS retrievals of temperature and ammonia in Jupiter's upper troposphere: implications for atmospheric dynamics, Bull. Am. Astron. Soc. 35, 997.

Atreya, S.K., Wong, M.H., Owen, T.C., Niemann, H.B., Mahaffy, P., 1997. Chemistry and clouds of the atmosphere of Jupiter: a Galileo perspective. In: Barbieri, C., Rahe, J., Johnson, T., Sohus, A. (Eds.), Three Galileos: The Man, The Spacecraft, The Telescope. Kluwer Academic Publishers, Dordrecht, pp. 249–260.

Atreya, S.K., Wong, M.H., Owen, T.C., Mahaffy, P.R., Niemann, H.B., de Pater, I., Drossart, P., Encrenaz, Th., 1999. A comparison of the atmospheres of Jupiter and Saturn: Deep atmospheric composition, cloud structure, vertical mixing, and origin. Planet. Space Sci. 47, 1243–1262.

Baines, K.H., Carlson, R.W., Kamp, L.W., 2002. Fresh ammonia ice clouds in Jupiter. Icarus 159, 74–94.

Brooke, T.Y., Knacke, R.F., Encrenaz, Th., Drossart, P., Crisp, D., Feuchtgruber, H., 1998. Models of the ISO 3-μm reflectance spectrum of Jupiter. Icarus 136, 1–13.

Clapp, M.L., 1995. Infrared spectroscopy and physical chemistry of cryogenic aerosols. Ph.D. Thesis, The University of North Carolina, Chapel Hill, NC.

Clapp, M.L., Miller, R.E., 1993. Shape effects in the infrared spectrum of ammonia aerosols. Icarus 105, 529–536.

de Pater, I., Dunn, D., Romani, P.N., Zahnle, K., 2001. Reconciling Galileo Probe data and ground-based radio observations of ammonia on Jupiter. Icarus 149, 66–78.

Edgington, S.G., Atreya, S.K., Trafton, L.M., Caldwell, J.J., Beebe, R.F., Simon, A.A., West, R.A., Barnet, C., 1998. On the latitude variation of ammonia, acetylene, and phosphine altitude profiles on Jupiter from HST Faint Object Spectrograph observations. Icarus 133, 192–209.

Flasar, F.M., 1986. Global dynamics and thermal structure of Jupiter's atmosphere. Icarus 65, 280–303.

Flasar, F.M., Kunde, V.G., Achterberg, R.K., Conrath, B.J., Simon-Miller, A.A., Nixon, C.A., Gierasch, P.J., Romani, P.N., Bézard, B., Irwin, P., Bjoraker, G.L., Brasunas, J.C., Jennings, D.E., Pearl, J.C., Smith, M.D., Orton, G.S., Spilker, L.J., Edberg, S.J., Carlson, R., Calcutt, S.B., Read, P.L., Taylor, F.W., Fouchet, T., Parrish, P., Barucci, A., Courtin, R., Coustenis, A., Gautier, D., Lellouch, E., Marten, A., Biraud, Y., Ferrari, C., Prangé, R., Owen, T.C., Abbas, M.M., Samuelson, R.E., Raulin, F., Ade, P., Césarsky, C.J., Grossman, K.U., Coradini, A., 2003. An intense stratospheric jet on Jupiter.

García-Melendo, E., Sánchez-Lavega, A., 2001. A study of the stability of Jovian zonal winds from HST images: 1995–2000. Icarus 152, 316–320.

Goody, R.M., Yung, Y.L., 1989. Atmospheric Radiation: Theoretical Basis, 2nd Edition. Oxford University Press, New York.

Kunde, V.R., Maguire, W.C., 1974. Direct integration transmittance model. J. Quant. Spectrosc. Radiat. Transfer 14, 803–817.

Kunde, V., et al., 1996. Cassini infrared Fourier spectroscopic investigation. In: Horn, L. (Ed.), Cassini/Huygens: A Mission to the Saturnian Systems. SPIE Proceedings Vol. 2803, The International Society for Optical Engineering, Bellingham, WA, pp. 162–177.

Lacis, A.A., Oinas, V., 1991. A description of the correlated k distribution method for modeling nongrey gaseous absorption, thermal emission, and multiple scattering in vertically inhomogeneous atmospheres. JGR 96: D5, 9027–9063.

Marten, A., Rouan, D., Baluteau, J.P., Gautier, D., Conrath, B.J., Hanel, R.A., Kunde, V., Samuelson, R., Chedin, A., Scott, N., 1981. Study of the ammonia ice cloud layer in the equatorial region of Jupiter from the infrared interferometric experiment on Voyager. Icarus 46, 233–248.

Martonchik, J.V., Orton, G.S., Appleby, J.F., 1984. Optical properties of $NH_3$ ice from the far infrared to the near ultraviolet. Appl. Opt. 23 (4), 541–547.

Mishchenko, M.I., Travis, L.D., 1998. Capabilities and limitations of a current FORTRAN implementation of the T-matrix method for randomly oriented, rotationally symmetric scatterers. J. Quant. Spectrosc. Radiat. Transfer 60 (3), 309–324.

Orton, G.S., Appleby, J.F., Martonchik, J.V., 1982. The effect of ammonia ice on the outgoing thermal radiance from the atmosphere of Jupiter. Icarus 52, 94–116.

Pope, S.K., Tomasko, M.G., Williams, M.S., Perry, M.L., Doose, L.R., Smith, P.H., 1992. Clouds of ammonia ice: Laboratory measurements of the single-scattering properties. Icarus 100, 203–220.

Roux, J.A., Wood, B.E., Smith, A.M., 1979. IR optical properties of thin $H_2O$, $NH_3$, and $CO_2$ cryofilms. AEDC-TR-79-57. Arnold Engineering Development Center, Tennessee.

Shaffer, W.A., Samuelson, R.E., Conrath, B.J., 1985. The vertical cloud structure of Jupiter's North Tropical Zone. Bull. Am. Astron. Soc. 17 (3), 706.

Shaffer, W.A., Samuelson, R.E., Conrath, B.J., 1986. Study of the ammonia ice cloud layer of the North Tropical Zone of Jupiter from the infrared interferometric experiment on Voyager. In: Allison, M., Travis, L.D. (Eds.), The Jovian Atmospheres. NASA Conference Publication 2441, pp. 64–70.

Smith, B.A., Soderblom, L.A., Johnson, T.V., Ingersoll, A.P., Collins, S.A., Shoemaker, E.M., Hunt, G.E., Masursky, H., Carr, M.H., Davies, M.E., Cook II, A.F., Boyce, J., Danielson, G.E., Owen, T., Sagan, C., Beebe, R.F., Veverka, J., Strom, R.G., McCauley, J.F., Morrison, D., Briggs, G.A., Suomi, V.E., 1979. The Jupiter system through the eyes of Voyager 1. Science 204, 13–32.

Smith, P.H., Tomasko, M.G., 1984. Photometry and polarimetry of Jupiter at large phase angles. II. Polarimetry of the south tropical zone, south equatorial belt, and the polar regions from the Pioneer 10 and 11 missions. Icarus 58, 35–73.

Waterman, P.C., 1971. Symmetry, unitarity, and geometry in electromagnetic scattering. Phys. Rev. D 3, 825–839.

Weidenschilling, S.J., Lewis, J.S., 1973. Atmospheric and cloud structure of the Jovian planets. Icarus 20, 465–476.

West, R.A., Strobel, D.F., Tomasko, M.G., 1986. Clouds, aerosols, and photochemistry in the Jovian atmosphere. Icarus 65, 161–217.

Wielaard, D.J., Mishchenko, M.I., Macke, A., Carlson, B.E., 1997. Improved T-matrix computations for large, nonabsorbing and weakly absorbing nonspherical particles and comparison with geometrical-optics approximation. Appl. Opt. 36: 18, 4305–4313.